

ARTICLE

OPEN



Manipulating the interlayer carrier diffusion and extraction process in organic-inorganic heterojunctions: from 2D to 3D structures

Jia-Wei Qiao¹, Wen-Qing Zhang¹, Feng-Zhe Cui¹, Hang Yin¹, Lin Feng¹ and Xiao-Tao Hao^{1,2}

Interlayer carrier transfer at heterointerfaces plays a critical role in light to electricity conversion using organic and nanostructured materials. However, how interlayer carrier extraction at these interfaces is poorly understood, especially in organic-inorganic heterogeneous systems. Here, we provide a direct strategy for manipulating the interlayer carrier diffusion process, transfer rate and extraction efficiency in tetracene/MoS₂ type-II band alignment heterostructure by constructing the 2D–3D organic-inorganic (O-I) system. As a result, the prolonged diffusion length (12.32 nm), enhanced electron transfer rate ($9.53 \times 10^9 \text{ s}^{-1}$) and improved carrier extraction efficiency (60.9%) are obtained in the 2D O-I structure which may be due to the more sufficient charge transfer (CT) state generation. In addition, we have demonstrated that the interlayer carrier transfer behavior complied with the diffusion mechanism based on the one-dimensional diffusion model. The diffusion coefficients have varied from 0.0027 to $0.0036 \text{ cm}^2 \text{ s}^{-1}$ as the organic layer changes from 3D to 2D structures. Apart from the relationship between the carrier injection and diffusion process, temperature-dependent time-resolved spectra measurement is used to reveal the trap-related recombination that may limit the interlayer carrier extraction. The controllable interlayer carrier transfer behavior enables O-I heterojunction to be optimized for optoelectronic applications.

npj 2D Materials and Applications (2022)6:2; <https://doi.org/10.1038/s41699-021-00278-1>

INTRODUCTION

Forming appropriate heterostructures has been a key concept in solid state science and an important tool to engineer the electronic and optical properties of semiconductors¹. Heterostructures formed by conventional semiconductors have led to some important discoveries, such as quantum spin hall effects^{2,3} and exciton-polariton condensations⁴. While, owing to the lattice-matching conditions required by the epitaxial growth, the lattice constants and crystal structures of the involved materials must be similar⁵. This severely limits the selection of materials and further development of the nanostructures.

The newly developed two-dimensional (2D) materials, such as graphene⁶, black phosphorus⁷, and transition metal dichalcogenides (TMDCs)⁸, provide diversified options to build heterostructures⁹. Importantly, TMDCs MX₂ (M = Mo, W; X = S, Se, Te) have garnered extensive attention in recent years owing to their strong light-matter interactions and extraordinary optoelectronic properties^{10–12}. As a result, monolayer TMDCs have been integrated with other materials to constitute van der Waals (vdW) heterostructures^{13–15}. The dangling-bond-free surface of 2D vdW materials not only can provide a platform for the efficient charge separation and transfer but also engineered the light-matter interaction and further explored potential applications for optoelectronic devices^{16,17}, including light-emitting diodes¹⁸, photodetectors¹⁹, solar cells²⁰, and field-effect transistors²¹.

With the rapid development of information technology, organic semiconductor materials were also an important alternative building block for vdW heterostructures, due to their advantages of diverse molecular structures, low cost, mechanical flexibility, and synthetic tunability^{22,23}. Recently, organic nanostructures using vdW interaction between 2D layered systems enable new applications^{24–26}. A phototransistor was obtained with broadband detection capability based on graphene/organic semiconductor

heterojunction²⁷. Various vertical organic-inorganic (O-I) heterojunctions have exhibited excellent rectifying behaviors as well as strong photovoltaic responses^{13,28}. To utilize the superior light-absorption and charge transfer (CT) properties of these vdW structures, photocarriers generated in the donor layer must transfer to the acceptor layer before recombination^{12,29}. Therefore, how to effectively control the O-I structure to achieve balanced interlayer carrier diffusion and injection process to achieve efficient carrier extraction has become a key issue to promote the further development of the O-I structure^{30,31}.

In this work, we illustrate the specific effects of dimensional changes in the O-I system, especially from the perspective of modulating the CT and exciton diffusion characteristics of the O-I interfaces. As a result, we have proved the controllable CT and carrier extraction process across the O-I interfaces with the heterojunction changed from 2D to 3D structures. The improved electron transfer rate and carrier extraction efficiency were obtained in the 2D O-I structure. The thickness-dependent exciton diffusion characteristics were observed in O-I heterostructures. In addition, the trap states observed from low-temperature PL spectra also play an important role in electron transfer and carrier recombination in tetracene/MoS₂ structure. Our work offers important guidance for preparing 2D vdW heterostructures with desirable band alignment, potentially leading to the realization of functional 2D photonic and optoelectronic devices.

RESULTS AND DISCUSSION

Construction and energy level arrangement of organic-inorganic heterojunction

To study the interlayer carrier transfer process, O-I layered heterostructures were selected as the research platform for the

¹School of Physics, State Key Laboratory of Crystal Materials, Shandong University, Jinan 250100 Shandong, China. ²ARC Centre of Excellence in Exciton Science, School of Chemistry, The University of Melbourne, Parkville, VIC 3010, Australia. email: lfeng@sdu.edu.cn; haoxt@sdu.edu.cn

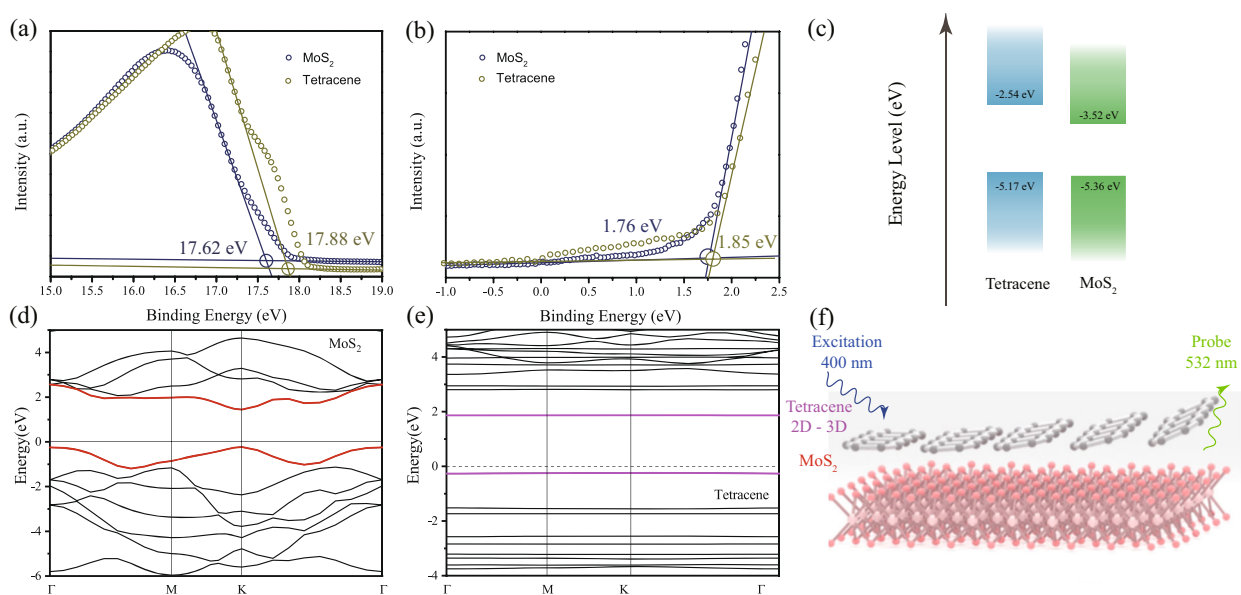


Fig. 1 Energy level arrangement and schematic image of O-I heterojunction. **a** UPS spectra of the secondary electron edge for monolayer MoS₂ and top organic layer tetracene. The extracted work functions for both structures are indicated, which are 3.58 and 3.32 eV, respectively. The work function was obtained by the equation: $\omega = h\nu - E_{\text{cut-off}}$. **b** UPS spectra at the low binding energy region near the Fermi level for monolayer MoS₂ and top organic layer tetracene. **c** The constructed band diagram of the tetracene/MoS₂ organic-inorganic vdW heterojunction. **d–e** The first principle DFT calculations of MoS₂ and tetracene, respectively. The calculation results confirmed that the tetracene/MoS₂ organic-inorganic heterostructure was Type-II band alignment. **f** Schematic configuration of tetracene/MoS₂ O-I vdW heterojunction.

interlayer carrier diffusion and transfer process because of their type-II band alignment³², which was further confirmed by using UV – vis absorption, ultraviolet photoelectron spectroscopy (UPS) measurements. As shown in Supplementary Figs. 1–2, by extrapolating the linear portion of the Tauc plot ($(ahv)^2$ versus hv), where a was the absorption coefficient and hv was the photon energy, the optical bandgap energy of monolayer MoS₂ was experimentally determined to be 1.84 eV, which was consistent with the theoretical prediction²¹. In addition, Fig. 1a shows plots of the secondary electron cut-off in the UPS spectra for the MoS₂ and tetracene layer, where the work function was extracted from the difference between photon energy (21.2 eV for He I photons) and photoemission onset (17.62 eV for MoS₂ and 17.88 eV for tetracene)³³. The values obtained from this analysis were 3.58 and 3.32 eV for MoS₂ and tetracene, respectively. Besides, from linear extrapolation of the onset of the low binding energy presented in Fig. 1b, the energy difference between the valence band edge (E_V) and E_F can be estimated at 1.76 eV for MoS₂ and 1.85 eV for tetracene. The E_F position of MoS₂ is closed to the edge of the conduction band, indicating highly electron-doped characteristics³⁴. As summarized in Fig. 1c, the energy band diagram of the monolithically formed O-I heterojunction exhibited typical features of type-II band alignment. Figure 1d, e show the energy bandgap of 1 L MoS₂ and tetracene by first-principle density functional theory (DFT) calculations, proving that the O-I heterostructure of tetracene and MoS₂ was type-II band alignment, which may lead to the dissociation of electrons and holes to the individual constituent layers in heterojunction¹⁵. The electrons in the upper layer of tetracene excited by 400 nm laser can be extracted by the bottom MoS₂ layer as shown in Fig. 1f.

Building of multidimensional organic-inorganic heterostructures and their exciton dynamics

Because the thickness of the donor tetracene layer in the heterostructures directly defined the length of the interlayer carrier transfer and diffusion process, building multidimensional

O-I heterostructures with various thicknesses is a straightforward approach to systematically understand the interlayer carrier transfer behavior. O-I heterostructures with varied thicknesses (keeping the MoS₂ as monolayer, Supplementary Fig. 3) were controllably prepared by a two-step method (detailed information was shown in Methods). All the organic layer thicknesses in this work were measured using atomic force microscopy (AFM) images, which were shown in Fig. 2a–c. The tetracene with a thickness of ca. 0.6 nm was referred to as 1 L, while the 10 nm thick film was referred to as bulk¹⁶. As a result, the increased organic layer thickness changed the O-I heterojunction from 2D structure to 3D structure. In addition, Raman spectroscopy was further carried out to confirm the TMDC_S and organic components of the heterojunctions (Supplementary Fig. 4a).

The steady-state absorption spectra of the heterojunction and the isolated components of the junction were shown in Fig. 2d. The three absorption maxima of the tetracene film, which were located at 443, 474 and 522 nm, can be attributed to the absorption from H- and J-aggregates, CT states, and associated vibrational sidebands, respectively⁸. The isolated MoS₂ spectrum included the B and A excitons at 605 nm and 651 nm, respectively. Distinctly, absorption enhancement was observed in the O-I heterojunction due to the higher absorption coefficient of the inorganic layer. Typical PL spectra collected from various organic layers were compared in Fig. 2e, the increased PL intensities owing to the increment of absorption (Supplementary Fig. 4b). The PL spectra acquired from tetracene and MoS₂ peaked at 532 nm and 668 nm, respectively (Supplementary Fig. 4c). In general, carriers in the donor layer can be efficiently extracted by the extraction layer during its lifetime which brings about dramatic quenching of the PL (Supplementary Fig. 5)³⁵. Comparing the spectral changes of the organic layer from 2D (0.6 nm) to 3D (bulk), no obvious peak broadening and shift are observed, indicating that the multi-dimensional organic structure has no obvious change of crystallinity affecting the optical properties (Supplementary Fig. 6a–b). Furthermore, the full width at half maxima measurement was also performed to exclude the

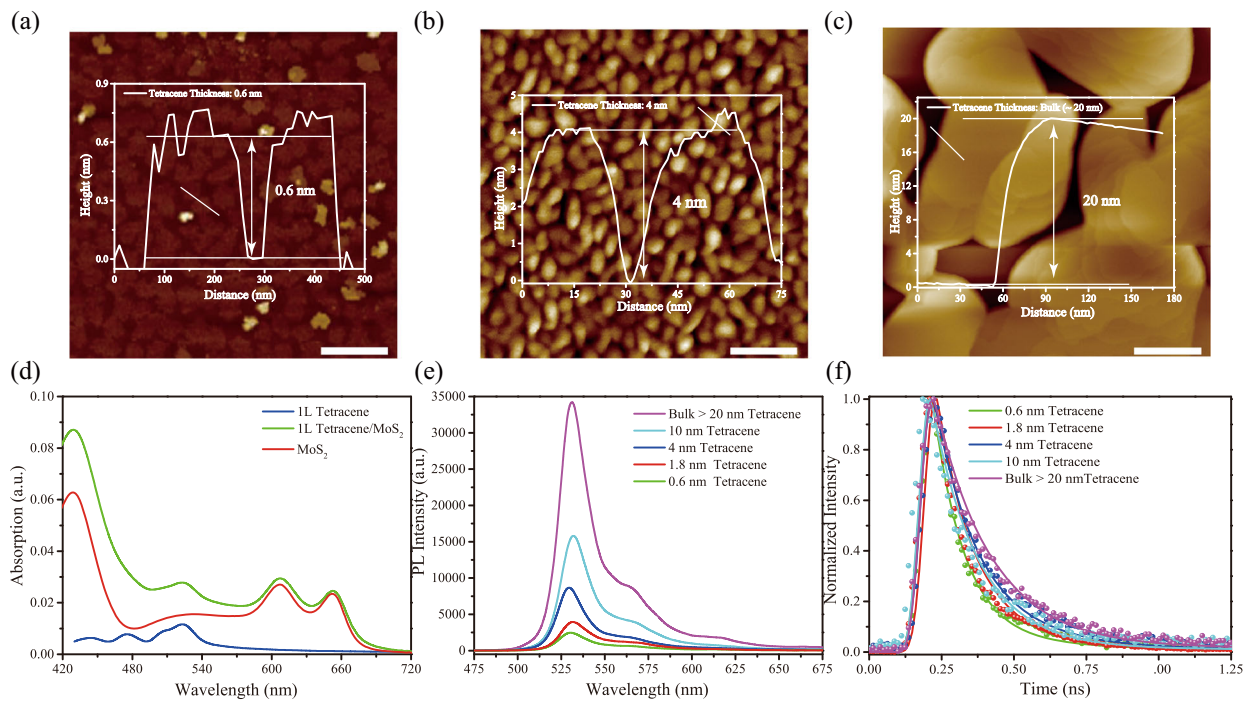


Fig. 2 Thicknesses and exciton dynamics characterizations of O-I heterojunction. **a** AFM image of 2D (0.6 nm) organic tetracene layer. The test area was indicated with the white line (scale bar: 500 nm). **b** AFM image of 4 nm organic tetracene layer. The test area was indicated with the white line (scale bar: 100 nm). **c** AFM image of bulk (>20 nm) organic tetracene layer. The test area was indicated with the white line (scale bar: 200 nm). **d** Steady-state absorption spectra of monolayer MoS_2 , tetracene and tetracene/ MoS_2 organic-inorganic heterostructure, respectively. **e** Steady-state PL spectra of tetracene layer with different thicknesses. **f** Normalized time-resolved PL decay profiles of tetracene layer with different thicknesses.

possibility that the PL intensity quenching originates from the defect states in tetracene layers of various thicknesses due to the laser irradiation-induced thermal decomposition³⁶. These results proved that the defect states do not change significantly with the thickness change. Distinct PL behaviors in different tetracene layers can be well interpreted by the excitonic dynamics processes. The TRPL measurements based on neat tetracene with different thicknesses were performed to accurately verify the potential CT process in the O-I heterojunction (Fig. 2f)³⁷. The lifetime data were fitted with the biexponential Eq. (1). For the O-I heterostructures, τ_1 and τ_2 are considered to be nonradiative and radiative lifetimes¹⁶. The detailed information was shown in Table 1 (Supplementary).

$$I = A \exp\left(-\frac{t}{\tau_1}\right) + B \exp\left(-\frac{t}{\tau_2}\right) \quad (1)$$

Interlayer exciton diffusion and carrier transfer process with various organic layer thickness

For these type II O-I heterostructures, electron carriers transfer from the upper layer (tetracene) to the bottom layer (MoS_2) after excitation³⁸. The DFT charge distribution calculations of 2D and 3D O-I heterostructures were shown in Fig. 3a, which proved that the organic tetracene layer was an excellent charge donor. Compared to the isolated tetracene with different thicknesses, the average lifetimes of tetracene (donor layer) in O-I heterostructures were decreased, which validates the CT process in the O-I system. For the 2D O-I heterojunction, significant fluorescence and lifetime quenching were observed (green and red lines in Fig. 3b). While, after the tetracene layer changed to the 3D structure (yellow and purple lines in Fig. 3b), the corresponding lifetime decreased from 318 ps to 294 ps at 532 nm and slight fluorescence quenching was observed in Supplementary Fig. 5b. These results indicated that

the existence of the faster and more efficient electron transfer process may originate from the 2D O-I system with the optimized nanoscale exciton separation. The related electron transfer rates (k_{ET}) of these blends were calculated using Eq. (2)³⁹.

$$k_{ET} = \frac{1}{\tau_{HS}} - \frac{1}{\tau_{neat}} \quad (2)$$

where τ_{neat} and τ_{HS} are the lifetime of neat tetracene and O-I heterostructures, respectively. For the 2D O-I heterojunction, the k_{ET} value of $6.07 \times 10^9 \text{ s}^{-1}$ was obtained, which was much longer than that of 3D structure ($2.57 \times 10^8 \text{ s}^{-1}$), as presented in Fig. 3c, which manifests the more efficient exciton dissociation and thus more sufficient CT state generation at the donor/acceptor interfaces. To further study the interlayer carrier transfer process, the carrier extraction efficiency was calculated as $\eta = \frac{\tau_{neat} - \tau_{HS}}{\tau_{neat}} \times 100\%$ (Fig. 3c). To make a fair comparison of O-I structures, we used 4.0–10.21 μW excitation light to explore the variation of extracted parameters. The results showed that the electron transfer rates and extraction efficiency remain stable with the change of excitation power (4.0–10.21 μW) for both 2D and 3D O-I structures (Supplementary Fig. 7). Supplementary Fig. 8a exhibited the significant overlap between the normalized absorption spectrum of tetracene and PL spectrum of MoS_2 , demonstrating the potential existence of Förster resonance energy transfer (FRET) in theory. In addition, we also probed the fluorescence decay time at 668 nm that was longer in the 2D O-I system than that in neat tetracene film, shown in Supplementary Fig. 8b. Therefore, we speculated that FRET occurred between the tetracene layer and MoS_2 layer⁴⁰.

To further study the relationship between the carrier transfer and extraction, the carrier diffusion dynamics of tetracene layer in O-I heterostructure was modeled by calculating the population and distribution of the carriers in tetracene layers using a one-dimensional diffusion equation as following

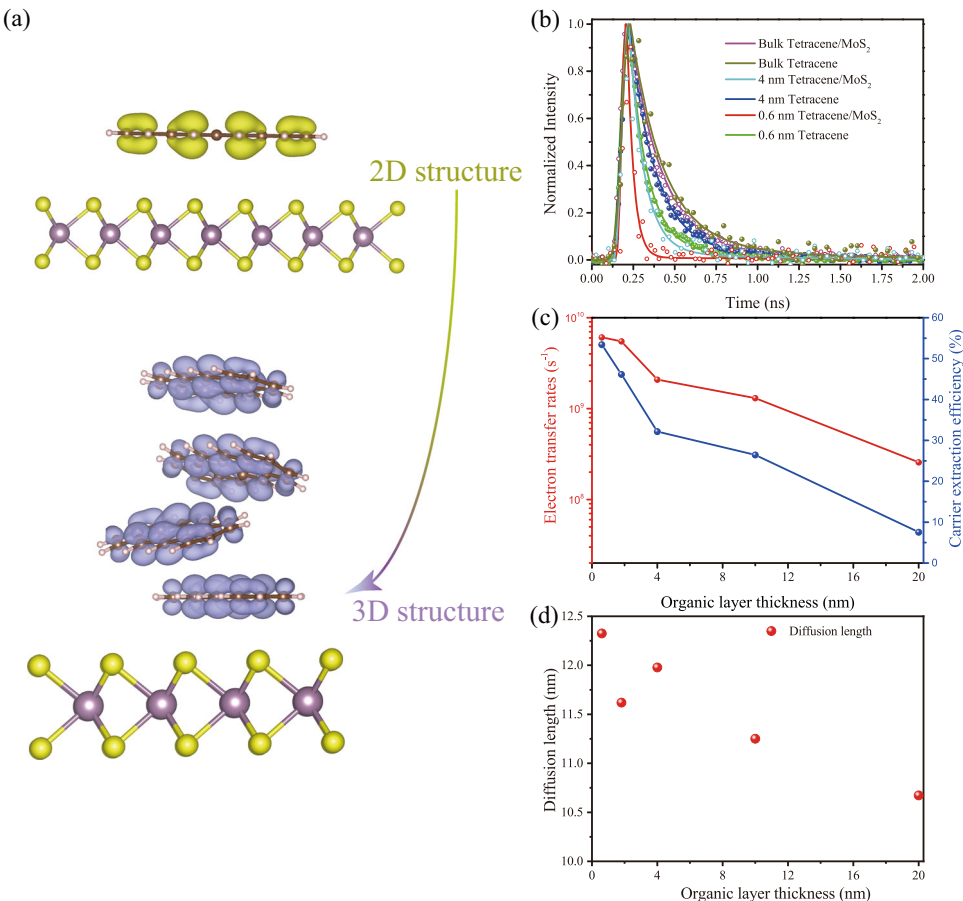


Fig. 3 Interlayer carrier transfer and exciton diffusion process with various organic layer thicknesses. **a** The DFT calculations of charge distribution from 2D to 3D organic-inorganic structures. **b** Normalized time-resolved PL decay profiles of tetracene layer in tetracene/MoS₂ heterostructures with various thicknesses. **c** The electron transfer rates (red line) and the carrier extraction efficiency (blue line) in tetracene/MoS₂ O-I heterojunction. **d** The results of the exciton diffusion length with different organic layer thicknesses.

equation (Eq. 3)^{41,42}:

$$\frac{\partial n(x, t)}{\partial t} = D \frac{\partial^2 n(x, t)}{\partial x^2} - \frac{n(x, t)}{\tau} \quad (3)$$

where D is the diffusion coefficient of tetracene, and τ represents the exciton lifetime across the sample, which was obtained by fitting the TRPL curve. $n(x, t)$ is the carrier population at x nm depth in the tetracene layers ($x=0$ at the upper surface), t the time delay, $n(0, t)=0$. Theoretical calculation of carrier density in the organic layer was shown in Note 1 (Supplementary). Based on this model, the TRPL curves of tetracene in heterostructures with different thicknesses were well fitted. The fitting results of D ranged from 0.0027 to $0.0036\text{ cm}^2\text{ s}^{-1}$ (Supplementary Fig. 9), which were consistent with the consequences of conventional organic materials⁴³. To better explore the relationship between the exciton diffusion and the organic layer thickness, we further investigated the diffusion length in 2D-3D O-I heterostructures as Eq. (4)⁴⁴:

$$L_D = \sqrt{Dt} \quad (4)$$

The diffusion length L_D was defined as a function of the diffusion time t_D and the diffusion coefficient D . In addition, the diffusion time t_D was the effective value of the intrinsic tetracene carrier lifetime, which can be obtained by fitting the TRPL curve of tetracene in the heterostructure with a bulk thickness (>40 nm, Supplementary Fig. 10)⁴⁴. When the thickness of the O-I heterostructure increased over 40 nm, the carrier extraction effect can be ignored. The results showed that the effective value of t_D was

422 ps. On the basis of Eq. (4), the results of diffusion length ranged from 10.7 nm to 12.32 nm were obtained (Fig. 3d). For the 20 nm organic layer thickness of heterojunction, the shortest diffusion length (10.7 nm) was observed. It was worth noting that for the 3D O-I heterojunction, the diffusion distance was significantly smaller than the thickness of the upper donor layer, which results in the unbalanced interlayer carrier diffusion and the extraction process, in good agreement with the results proved in Fig. 3c. In addition, the exciton-exciton annihilation effect may be increased as the thickness of the organic layer increased, which may limit the exciton diffusion and carrier transfer process in the O-I system⁴⁵.

Thermal field regulated interlayer carrier transfer behaviors

The interlayer carrier transfer behavior was also sensitive to the temperature. By decreasing the temperature, the intensities of PL characteristics increased due to the decreased phonon interaction. In the temperature-dependent PL spectra of MoS₂ (Supplementary Fig. 11a), an obvious blue shift was observed, which may be attributed to the broadening of the energy bandgap and exciton confinement by the weak phonon interaction⁴⁶. The temperature-dependent energy bandgap extension can be described as $E_g = E_0 - \alpha T^2/(T + \beta)$, where E_g was the energy bandgap, E_0 was its value at 0 K, α and β were proportionality constants⁴⁷. Figure 4a, b show the temperature-dependent steady-state PL spectra of the pristine 1 L (0.6 nm) tetracene and 3D tetracene, respectively. For the pristine tetracene structure, new PL peaks in the range of 700–760 nm were observed, indicating the formation

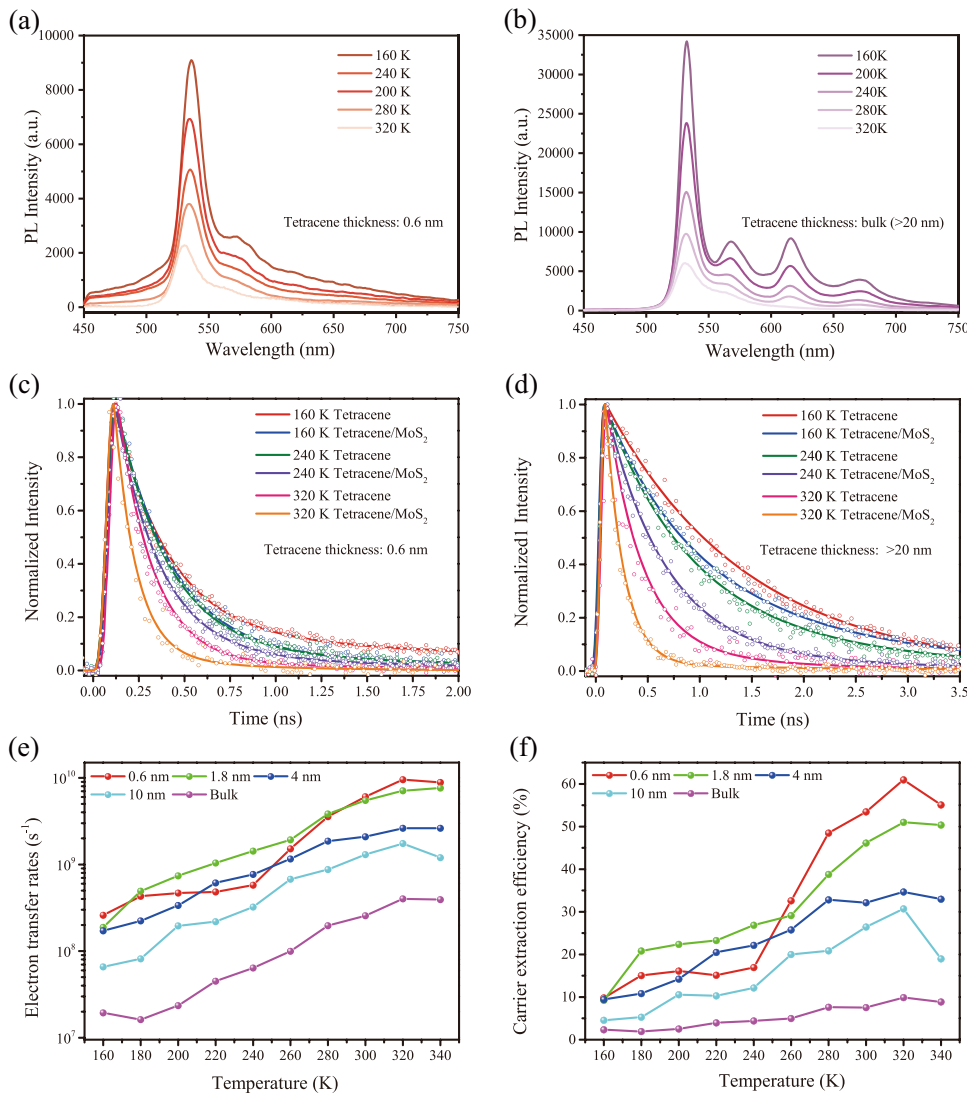


Fig. 4 Temperature-dependent interlayer carrier dynamic characteristics. **a** Steady-state PL spectra of 2D tetracene layer from 160 to 320 K. **b** Steady-state PL spectra of 3D tetracene layer from 160 to 320 K. **c** The results of the time-resolved spectra of tetracene in isolated 1 L tetracene and 2D tetracene/MoS₂ structures at 160 K, 240 K and 320 K, respectively. **d** The results of the time-resolved spectra of tetracene in isolated bulk tetracene and 3D tetracene/MoS₂ structures at 160 K, 240 K and 320 K, respectively. **e** The results of the temperature-dependent electron transfer rates with different organic layer thicknesses. **f** The results of the temperature-dependent carrier extraction efficiency with different organic layer thicknesses.

of trap states at low temperature (Supplementary Fig. 11b)⁸. The bound excitons originated from trap states were caused by impurities and defects on the surface, resulting in the broadening of the PL spectrum.

To better analyze the influence of the trap states of different O-I structures, the temperature-dependent time-resolved spectra were measured, as shown in Fig. 4c, d. Compared with the tetracene lifetime at room temperature, a significant lifetime increase was observed for all organic layer thickness under low-temperature conditions. Besides, clearer biexponential decay was observed with the temperature decreased due to the trap-related recombination. Compared to the isolated tetracene with different thicknesses, the average lifetimes of tetracene in O-I heterostructures were decreased at the same temperature, which proves the CT process in the O-I system. For the O-I structure with the 2D tetracene layer, we observed a more significant lifetime quenching phenomenon of the donor layer, which is consistent with the aforementioned results at room temperature (Fig. 3b). In addition, the increased lifetime of the organic layer may be originated from

exciton fission⁴⁸, which is expected to slow the electron-hole recombination. Like Eq. (2), the related electron transfer rates of these hybrid O-I heterojunctions were measured to describe the temperature-dependent CT process (Fig. 4e). By changing the temperature from 160 to 340 K, the electron transfer rates increased from $2.60 \times 10^8 \text{ s}^{-1}$ to $9.53 \times 10^8 \text{ s}^{-1}$ for the 2D O-I heterostructure. For all thicknesses of heterojunctions, the lowest electron transfer rates were obtained at 160 K. Besides, the trap states also limited the carrier transfer and carrier extraction at the donor/acceptor interfaces leading to the decreased carrier extraction efficiency at lower temperatures (Fig. 4f). The detailed information about the temperature-dependent lifetime with various organic layer thicknesses was shown in Table 1 (Supplementary).

In summary, we have observed the controllable interlayer carrier transfer and extraction process successfully in multi-dimensional type-II band alignment vdW heterostructures with tetracene and monolayer MoS₂. Apart from the controllable carrier transfer research, the thickness-dependent exciton diffusion

process was also observed by ultrafast spectroscopy. Due to the balanced interlayer carrier diffusion and injection process, the highest electron transfer rate ($9.53 \times 10^9 \text{ s}^{-1}$) was obtained in the 2D O-I structure. Furthermore, the electron transfer process was also sensitive to the temperature due to the formation of trap states at low temperatures, which caused the trap-related recombination and limited carrier extraction. Our findings provide a facile and general way to manipulate the light-matter interaction in 2D materials and to control the CT across O-I interfaces in hybrid systems, enabling new possibilities and innovations in future optoelectronic applications.

METHODS

Materials

Monolayer MoS₂ on SiO₂/Si substrates was purchased from SixCarbon Technology Shenzhen Inc. Tetracene was purchased from tetracene TCI Technology.

Preparation of organic-inorganic heterostructures

Tetracene/MoS₂ O-I heterojunction was fabricated in two steps. The monolayer MoS₂ that we used in this work was grown on a 300 nm Si/SiO₂ substrate by the chemical vapor deposition (CVD) method. The tetracene films with different thicknesses were subsequently grown on the monolayer MoS₂ via the physical vapor deposition method. The deposition rate was 0.01 nm s^{-1} and the vacuum was held to $2.0 \times 10^{-4} \text{ Pa}$ at 215°C . The thickness of bulk-tetracene was over 10 nm. All the tetracene layer thickness in this work were measured using the AFM images.

DFT calculation

DFT calculations were carried out using the Quantum Espresso package. Projector-augmented-wave potentials were adopted to describe the electron-ion interactions, and the generalized gradient approximation in the form of the Perdew–Burke–Ernzerhof functional was employed to treat the electron exchange-correlation. The energy cut-off for plane-wave basis was set to 500 eV. The convergence threshold for the iteration in the self-consistent field and the maximum force component for geometry optimizations were set to 10^5 eV and 0.01 eV \AA^{-1} , respectively. The k-point sampling of the Brillouin zone was carried out using a $3 \times 3 \times 1$ and $7 \times 7 \times 1$ k-point grid for structural optimizations and energy calculations, respectively.

Characterization

The absorption was characterized with the TU-1900 UV-vis dual-beam spectrophotometer (PG Instruments, Ltd.). The absorption spectra of MoS₂ were obtained by transferring the monolayer MoS₂ to the quartz substrate. The steady-state PL spectra and TRPL spectra were acquired through a confocal optical microscope (Nanofinder FLEX2, Tokyo Instruments, Inc.) equipped with time-correlated single-photon counting (TETRACENESP) module (Becker & Hickl, SPC-150). All the PL spectra were measured using a charge-coupled device sensor (DU420A-OE, Andor) to select the different regions across the samples. Topography images were obtained using AFM in tapping mode (Solver P47 PRO, NTMDT Co.). Raman measurement was conducted using Micro Raman spectrometer LabRAM HR800 (Renishaw plc).

DATA AVAILABILITY

The data that support the findings of this study are available from the corresponding author upon reasonable request.

Received: 19 August 2021; Accepted: 1 December 2021;

Published online: 12 January 2022

REFERENCES

- Cai, Z., Liu, B., Zou, X. & Cheng, H. M. Chemical Vapor Deposition Growth and Applications of Two-Dimensional Materials and Their Heterostructures. *Chem. Rev.* **118**, 6091–6133 (2018).
- Von Klitzing, K. Essay: quantum hall effect and the new international system of units. *Phys. Rev. Lett.* **122**, 200001 (2019).
- Canonica, L. M., Rappoport, T. G. & Muniz, R. B. Spin and Charge Transport of Multiorbital Quantum Spin Hall Insulators. *Phys. Rev. Lett.* **122**, 196601 (2019).
- Gao, T. et al. Talbot Effect for Exciton Polaritons. *Phys. Rev. Lett.* **117**, 097403 (2016).
- Pei, J. et al. Excited State Biexcitons in Atomically Thin MoSe₂. *ACS Nano* **11**, 7468–7475 (2017).
- Liu, B., Abbas, A. & Zhou, C. Two-dimensional semiconductors: from materials preparation to electronic applications. *Adv. Electron. Mater.* **3**, 1700045 (2017).
- Zong, X. et al. Black phosphorus-based van der Waals heterostructures for mid-infrared light-emission applications. *Light. Sci. Appl.* **9**, 114 (2020).
- Park, H. J. et al. Hybrid Characteristics of MoS₂ Monolayer with Organic Semiconducting Tetracene and Application to Anti-Ambipolar Field Effect Transistor. *Acs. Appl. Mater. Interfac.* **10**, 32556–32566 (2018).
- Wang, H. et al. Van der Waals Integration Based on Two-Dimensional Materials for High-Performance Infrared Photodetectors. *Adv. Funct. Mater.* **31**, 2103106 (2021).
- Zheng, W. et al. Direct Vapor Growth of 2D Vertical Heterostructures with Tunable Band Alignments and Interfacial Charge Transfer Behaviors. *Adv. Sci.* **6**, 1802204 (2019).
- Roy, T. et al. 2D-2D tunneling field-effect transistors using WSe₂/SnSe₂ heterostructures. *Appl. Phys. Lett.* **108**, 083111 (2016).
- Hong, X. et al. Ultrafast charge transfer in atomically thin MoS₂/WS₂ heterostructures. *Nat. Nanotechnol.* **9**, 682–686 (2014).
- Lee, J. Y., Shin, J. H., Lee, G. H. & Lee, C. H. Two-Dimensional Semiconductor Optoelectronics Based on van der Waals Heterostructures. *Nanomaterials-based* **6**, 193 (2016).
- Geim, A. K. & Grigorieva, I. V. Van der Waals heterostructures. *Nature* **499**, 419–425 (2013).
- Jin, C. et al. Ultrafast dynamics in van der Waals heterostructures. *Nat. Nanotechnol.* **13**, 994–1003 (2018).
- Zhang, L. et al. Efficient and Layer-Dependent Exciton Pumping across Atomically Thin Organic-Inorganic Type-I Heterostructures. *Adv. Mater.* **30**, 1803986 (2018).
- Li, Z. et al. Intercalation Strategy in 2D Materials for Electronics and Optoelectronics. *Small Methods* **5**, 2100567 (2021).
- Parveen, S., Paul, K. K. & Giri, P. K. Precise Tuning of the Thickness and Optical Properties of Highly Stable 2D Organometal Halide Perovskite Nanosheets through a Solvothermal Process and Their Applications as a White LED and a Fast Photodetector. *Acs. Appl. Mater. Interfac.* **12**, 6283–6297 (2020).
- Lopez-Sanchez, O., Lembke, D., Kayci, M., Radenovic, A. & Kis, A. Ultrasensitive photodetectors based on monolayer MoS₂. *Nat. Nanotechnol.* **8**, 497–501 (2013).
- Lin, Y. et al. 17% Efficient Organic Solar Cells Based on Liquid Exfoliated WS₂ as a Replacement for PEDOT:PSS. *Adv. Mater.* **31**, 1902965 (2019).
- Wu, B. et al. Multifunctional MoS₂ Transistors with Electrolyte Gel Gating. *Small* **16**, 2000420 (2020).
- Cheng, C. H., Li, Z., Hambarde, A. & Deotare, P. B. Efficient Energy Transfer across Organic-2D Inorganic Heterointerfaces. *Acs. Appl. Mater. Interfac.* **10**, 39336–39342 (2018).
- Wang, S. et al. A MoS₂/PTCDA Hybrid Heterojunction Synapse with Efficient Photoelectric Dual Modulation and Versatility. *Adv. Mater.* **31**, 1806227 (2019).
- Kakavelakis, G. et al. Size-Tuning of WSe₂ Flakes for High Efficiency Inverted Organic Solar Cells. *ACS Nano* **11**, 3517–3531 (2017).
- Lyu, C. K. et al. Functionalized Graphene Oxide Enables a High-Performance Bulk Heterojunction Organic Solar Cell with a Thick Active Layer. *J. Phys. Chem. Lett.* **9**, 6238–6248 (2018).
- Pei, K. & Zhai, T. Emerging 2D Organic-Inorganic Heterojunctions. *Cell Rep. Phys. Sci.* **1**, 100166 (2020).
- Han, J. et al. Graphene/Organic Semiconductor Heterojunction Phototransistors with Broadband and Bi-directional Photoresponse. *Adv. Mater.* **30**, 1804020 (2018).
- Hu, F. et al. Tailored Plasmons in Pentacene/Graphene Heterostructures with Interlayer Electron Transfer. *Nano Lett.* **19**, 6058–6064 (2019).
- Li, H. et al. Recent progress and strategies in photodetectors based on 2D inorganic/organic heterostructures. *2D Mater.* **8**, 012001 (2020).
- Wu, H. et al. MoS₂/C/C nanofiber with double-layer carbon coating for high cycling stability and rate capability in lithium-ion batteries. *Nano Res.* **11**, 5866–5878 (2018).
- Habib, M. R. et al. Tunable photoluminescence in a van der Waals heterojunction built from a MoS₂ monolayer and a PTCDA organic semiconductor. *Nanoscale* **10**, 16107–16115 (2018).
- Bettis Homan, S. et al. Ultrafast Exciton Dissociation and Long-Lived Charge Separation in a Photovoltaic Pentacene-MoS₂ van der Waals Heterojunction. *Nano Lett.* **17**, 164–169 (2017).

(ZR2019ZD43). L.F. thanks Natural Science Foundation of Shandong Province for the grant of ZR2019MA069. X.T.H. also acknowledges support from the ARC Centre of Excellence in Exciton Science (CE170100026).

AUTHOR CONTRIBUTIONS

J.W.Q., L.F., and X.T.H. conceived the idea and performed the data analysis. J.W.Q., F.Z. C., and Y.H. conducted the characterization and measurement of the materials. W.Q.Z. provided the first principle DFT calculation. J.W.Q., L.F., and X.T.H. Hao co-wrote the paper. All authors discussed the results and commented on the paper.

COMPETING INTERESTS

The authors declare no competing interests.

ADDITIONAL INFORMATION

Supplementary information The online version contains supplementary material available at <https://doi.org/10.1038/s41699-021-00278-1>.

Correspondence and requests for materials should be addressed to Lin Feng or Xiao-Tao Hao.

Reprints and permission information is available at <http://www.nature.com/reprints>

Publisher's note Springer Nature remains neutral with regard to jurisdictional claims in published maps and institutional affiliations.



Open Access This article is licensed under a Creative Commons Attribution 4.0 International License, which permits use, sharing, adaptation, distribution and reproduction in any medium or format, as long as you give appropriate credit to the original author(s) and the source, provide a link to the Creative Commons license, and indicate if changes were made. The images or other third party material in this article are included in the article's Creative Commons license, unless indicated otherwise in a credit line to the material. If material is not included in the article's Creative Commons license and your intended use is not permitted by statutory regulation or exceeds the permitted use, you will need to obtain permission directly from the copyright holder. To view a copy of this license, visit <http://creativecommons.org/licenses/by/4.0/>.

© The Author(s) 2022

33. Zhou, Y. et al. Unraveling the Role of Substrates on Interface Energetics and Morphology of PCDTBT:PC₇₀BM Bulk Heterojunction. *Adv. Mater. Interfac.* **2**, 1500095 (2015).
34. Hu, Z., Liu, Z. B. & Tian, J. G. Stacking of exfoliated two-dimensional materials: a review. *Chin. J. Chem.* **38**, 981–995 (2020).
35. Qiao, J.-W. et al. Efficient photoluminescence enhancement and tunable photocarrier transfer in vertical 2D organic-inorganic heterostructure by energy funneling. *2D Mater.* **8**, 025026 (2021).
36. Dang, J. et al. Identifying defect-related quantum emitters in monolayer WSe₂. *npj 2D Mater. Appl.* **4**, 2 (2020).
37. Zheng, F. et al. Purified dispersions of graphene in a nonpolar solvent via solvothermal reduction of graphene oxide. *Chem. Commun.* **51**, 3824–3827 (2015).
38. Cheng, C. H., Li, Z., Hambardze, A. & Deotare, P. B. Efficient Energy Transfer across Organic-2D Inorganic Heterointerfaces. *ACS Appl. Mater. Interfac.* **10**, 39336–39342 (2018).
39. Zhang, K.-N. et al. High-Performance Ternary Organic Solar Cells with Morphology-Modulated Hole Transfer and Improved Ultraviolet Photostability. *Sol. RRL* **4**, 2000165 (2020).
40. Xu, W.-L. et al. Förster Resonance Energy Transfer and Energy Cascade in Broadband Photodetectors with Ternary Polymer Bulk Heterojunction. *J. Phys. Chem. C* **119**, 21913–21920 (2015).
41. Qi, P. et al. Remote Lightening and Ultrafast Transition: Intrinsic Modulation of Exciton Spatiotemporal Dynamics in Monolayer MoS₂. *ACS Nano* **14**, 6897–6905 (2020).
42. Kulig, M. et al. Exciton Diffusion and Halo Effects in Monolayer Semiconductors. *Phys. Rev. Lett.* **120**, 207401 (2018).
43. Zhang, K.-N. et al. Exploring the mechanisms of exciton diffusion improvement in ternary polymer solar cells: from ultrafast to ultraslow temporal scale. *Nano Energy* **79**, 105513 (2021).
44. Zheng, W. et al. Probing and Manipulating Carrier Interlayer Diffusion in van der Waals Multilayer by Constructing Type-I Heterostructure. *Nano Lett.* **19**, 7217–7225 (2019).
45. Linardy, E. et al. Harnessing Exciton-Exciton Annihilation in Two-Dimensional Semiconductors. *Nano Lett.* **20**, 1647–1653 (2020).
46. Podzorov, V. et al. Intrinsic charge transport on the surface of organic semiconductors. *Phys. Rev. Lett.* **93**, 086602 (2004).
47. Hatch, R. C., Huber, D. L. & Hochst, H. Electron-phonon coupling in crystalline pentacene films. *Phys. Rev. Lett.* **104**, 047601 (2010).
48. Diroll, B. T., Zhou, H. & Schaller, R. D. Low-Temperature Absorption, Photoluminescence, and Lifetime of CsPbX₃ (X = Cl, Br, I) Nanocrystals. *Adv. Funct. Mater.* **28**, 1800945 (2018).

ACKNOWLEDGEMENTS

This work was supported by the National Natural Science Foundation of China (11774204) and Major Program of Natural Science Foundation of Shandong Province